Silicon (2024) 16:4915–4928
https://doi.org/10.1007/s12633-024-03057-x

RESEARCH

Modelling Studies of Rotary Magnetic Field in ECDM for Microchannel Fabrication of Silica Glass

Dilip Gehlot[1] · Pradeep Kumar Jha[1] · Pramod Kumar Jain[1]

Received: 28 March 2024 / Accepted: 5 June 2024 / Published online: 13 June 2024

Abstract
Recent developments in the fabrication of microfluidic channels of silica glass require repeatability and surface integrity for the industrial purpose of the ECDM process, which is made possible by controlling the dynamic parameters during machining. The characteristics of gas film, i.e., nucleation growth and bubble departure away from the tool, play a vigorous role in enhancing the quality characteristics of ECDM. MHD convection induced by a rotary magnetic field precisely regulates the gas film characteristics. It improves the ejection of particles at higher depths after chemical etching, which enhances the machining capability to fabricate a high aspect ratio microchannel. Various researchers have already done work by applying static magnetic fields in the ECDM process for micro-drilling. This work uses the novel approach of the rotary magnetic field in the electrochemical discharge machining process to fabricate microchannels using an in-house fabricated RMAECDM (Rotary magnetic field assisted ECDM) setup. The percentage reduction in the width overcut obtained by a rotary magnetic field compared to conventional ECDM and static magnetic field application is 21% and 8 %, respectively, under the same environments. Nature-inspired algorithms, coupled with Taguchi techniques, were applied to find the optimal setting of input parameters. The optimal voltage setting, concentration, field rotation, and magnetic strength are 40V,20%, 20000 RPM, and 220mT.

Keywords Optimization · Discharge · Nature-inspired · MHD · Overcut

1 Introduction

The miniature components, i.e., syringes pumps, micro blowers, and nanofluidic mixtures, are utilized in medical instruments, space, and chemical industries. Nonconductive materials, i.e., glass, ceramics, and quartz, are extensively used to fabricate microfluidic channels. ECDM is an appropriate process to machine the nonconductive brittle material, which is difficult in conventional methods [1]. It is a hybrid process that combines electrochemical and electro-discharge to perform various operations like drilling, turning, and milling. These operations are known as electrochemical discharge drilling [2], electrochemical discharge milling [3], electrochemical discharge turning [4], WECDM [5], die-sinking electrochemical discharge machining [6], and electrochemical discharge trepanning [7]. Chemical etching and high-temperature melting are utilized to remove material in this process. Many scientists have investigated ECDM and stated how numerous electrical variables, discharge phenomena, tools, and workpiece materials affect processing. Recent studies in micromachining have focused on ECDM, which has developed as a feasible alternative method for micromachining glass materials because of low cost, process flexibility, and relatively better surface qualities [8]. It is the hybridization of ECM and EDM since the electrochemical reaction is required to initiate the discharge that supports the chemical etching [9]. High-temperature chemical etching is the primary mechanism of material removal. When the electrochemical reactions start, water molecules disassociate into H and OH ions that move toward the electrodes [10]. H ions strike with the electrons near the cathode, forming hydrogen gas. Electrons generate hydrogen gas whenever the electric double-layer capacitor is charged reasonably, and the

✉ Dilip Gehlot
dilip_g@me.iitr.ac.in

Pradeep Kumar Jha
pradeepjha@me.iitr.ac.in

Pramod Kumar Jain
pkjain@gmail.com

[1] Department of Mechanical and Industrial Engineering, Indian Institute of Technology, Roorkee, India

bubble nucleates in the supersaturation state [11]. It adheres, grows, and moves away with a larger diameter in the adhesion, diffusion, and bulk stages of bubble formation [12]. The bubble detaches whenever the buoyancy force surpasses the surface tension [13]. Departure diameter continuously increases, which isolates the tooltip from the electrolyte [14]. It is independent of current density and only varies with the buoyancy force and viscosity of the electrolyte [15]. Some improvements in heat-affected zones and overcuts are observed by applying non-Newtonian electrolyte fluid [16]. Different kinds of energy are applied to regulate the bubble growth and gas film formation cycle. The triplex hybrid methods were developed by combining different forms of energy to improve the performance characteristics. Many researchers significantly contributed to the improvements of ECDM such as rotary ECDM [17], powder-mixed ECDM [18], ECDG [19], magnetic-field-assisted ECDM [20], and vibration-assisted ECDM [21]. Vibration-assisted electrochemical discharge drilling was proposed to improve the discharge stability and machining quality. A significant effect of vibration frequency and amplitude on gas film characteristics was observed [22]. In addition, ultrasonic-assisted electrochemical discharge milling was also developed to refine the gas film thickness, optimize the energy distribution, and stabilize the current signal. The process becomes more capable of fabricating microchannels with good surface finish under the influence of ultrasonic vibration [23]. A multiphase-injection system (MIS) attaches with the ECDM to enhance electrolyte flushing action. Thermal damage near the entrance of the micro-hole decreases due to stable and consistent discharge by the MIS system [24]. Hybridizing magnetic flux with the ECDM process is one of the ways to manage bubble formation and departure cycle by exerting magnetohydrodynamic convection (MHD) in the electrolytic cell [25]. Deep micro-drilling always encounters a problem in the ECDM process due to improper entrance of electrolytes in the tool-workpiece gap. Since the voltage and duty cycle variation cannot prevent the nucleation growth and departure of the bubble. Magnetic flux persuades the magnetic hydrodynamic convection, which provides a steering effect [26]. Modelling studies of MHD convection, which explains the role of the magnetic field on the bubble departure radius, were discussed [27]. Magnetic flux influences the gas film formation and various stages of bubble formation by moving the bubbles away from the tool edge [28]. Bubble entrapment was reduced using the multitap array tool (MTA), in which tip length and pitch size of MTA were considered critical parameters affecting entrapment's severity [29]. The mass transfer phenomena, reaction kinetics, and deposition quality also improved due to the movements of the charged particle under the influence of the MHD convection [30]. The orientation of the magnetic field also enhances the machining performance since bubble movements also change with the variation of orientation [26]. Micro-sit of higher machining depth (more than 1000 microns) was also fabricated with the association of magnetic field in the ECDM process [31]. The major problem with the ECDM process is the availability of the electrolyte solution at the working site with increasing depth of the micro-channel since the debris cannot move away from the gap, and no fresh electrolytes interact in the machining zone. The machining zone is divided into hydrodynamic and discharge regimes under the tooltip. The discharge regime exists up to 300 microns depth, and the machining operation is mainly a function of discharge characteristics in this regime. Beyond that, the hydrodynamic regime starts, and the discharge characteristics deteriorate due to the accumulation of machined by-products, i.e., sludge, salts, and debris, followed by H2 bubbles at the hole entrance. Therefore, machining performance in this region depends on the hydrodynamic characteristic instead of discharge. The hydrogen bubble accumulation prevents the interaction of fresh electrolytes in the machining zone. It generates discharge at the entrance instead of the bottom of the hole, resulting in inaccuracy in the machined profile. Therefore, forming a hydrodynamic regime should be prevented for better machining accuracy. It also influences the machining rate and increases the localized temperature, spreading the thermal cracks [32]. The other problem encountered during microfabrication is an unstable gas film that prevents reproducibility. This problem is removed by minimizing gas film thickness and decreasing the bubble departure time, which drops critical voltage, and machining starts with a slightly lower voltage. In some cases, precise control of spark and gas film formation is done by the side insulation of the tool. It generates a stable spark compared to an uninsulated tool [33]. NSGA-II techniques were also applied with the hybridization of RSM to find the optimal setting of controllable factors [34].

The gas film characteristic is the leading factor that decides the quality, repeatability, surface finish, and machining rate. The rotating tool helps to stabilize the bubble formation cycle and maintain a uniform spark [35, 36]. In some of the literature, ultrasonic vibration is added to reduce film thickness and increase the number of discharges in the single pulse [37, 38]. The association of a magnetic field with ECDM also improves the material removal rate [39]. At a higher machining depth, inadequate moistening of the electrode is due to machined particles, which are difficult to separate from the hole. Stable gas film and proper electrolyte circulation in the gap are the ECDM primary requirements. The MHD approach is applied to improve the process parameters and accuracy of the ECDM process for microfeature fabrication. Apart from these, some authors also studied the effect of tool shape and wettability on process characteristics. The surface roughness of the tool decides the wettability, which

influences gas film formation due to the increase in surface tension of the bubble adhered to the tool [40]. Due to the absence of a fringing effect, the conical shape tool provides a more consistent spark than the cylindrical tool shape [41].

Abundant work has been done to find the voltage, concentration, and duty cycle ratio outcome on accuracy and quality factors. A few pieces of literature are available to enumerate the impact of applying the MHD convection into the gas bubble formation cycle, surface roughness, and machining rate. In this work, the primary focus is to examine the impact of the rotary magnetic flux on the machining performance, which was not reported in the available literature. The work done by various researchers discusses the outcome of a static magnetic flux on the process parameters. Therefore, this work applies a rotating magnetic field to fabricate a microfluidic channel and also discusses the effect of magnetic field rotation speed on the MRR and WOC. The paper also contains the systematic procedure for a couple of physics involved, i.e., the Laplace equation for potential distribution, magnetic field distribution, and flow simulation under MHD convection. The rotating magnetic field is obtained by spinning a permanent magnet with the help of a DC motor. The variation in magnetic field strength and rotation influences the hydrodynamic regime characteristics. When the current flows in the electrolyte in the presence of a magnetic field, the Lorentz force generates MHD convection. Due to this effect, the bubble moves away from the tip and decreases the departure radius. The rotating magnetic field induces the alternating magnetic field strength, which gives sufficient time for the electrolytic ions to participate in the electrochemical reaction whenever the fresh electrolyte comes in contact with the tool edge.

2 Material and Methods

The different parts of RMAECDM (Fig. 1a) are a power supply, stepper motor for axial table movements, DC motor for tool rotation, and workpiece fixture. A rotating magnetic field is generated through the DC motor and the specially designed fixture for holding the permanent magnet (Nd-Fe-B) of 220 mT and 320 mT field strength measured by a gaussmeter. Magnetic flux intensity and Lorentz force due to MHD convection are also shown in Fig. 1. When the critical voltage grasps the threshold to initiate an electrochemical reaction, a small bubble will be generated, slowly growing into big ones. Electrodes bounded with a gas film with the accumulation and coalescence of the bubble.

As voltage reaches a critical value, the gas film will be broken down, and a discharge occurs (Fig. 2a). As part of the discharge energy's contact with the workpiece, localized melting takes place, which leaves a pit on the workpiece's surface. The experiments were also conducted at varying magnetic field speeds using a speed regulator to elaborate the effect of changing magnetic field speeds with quality characteristics. The rotary magnetic field encourages the steering effect on the bubbles, enhancing machining performance characteristics. The role of the rotary magnetic field in spark formation is to form thin and uniform gas film, reduce the breakdown voltage, and thus form the spark at lower voltage. Due to Lorentz's force, the combination of electrical potential and magnetic flux in the interelectrode gap achieves the steering action of electrolytes and bubbles.

The magnetic field strength and rotation speed can govern the intensity of steering action. Convection caused by

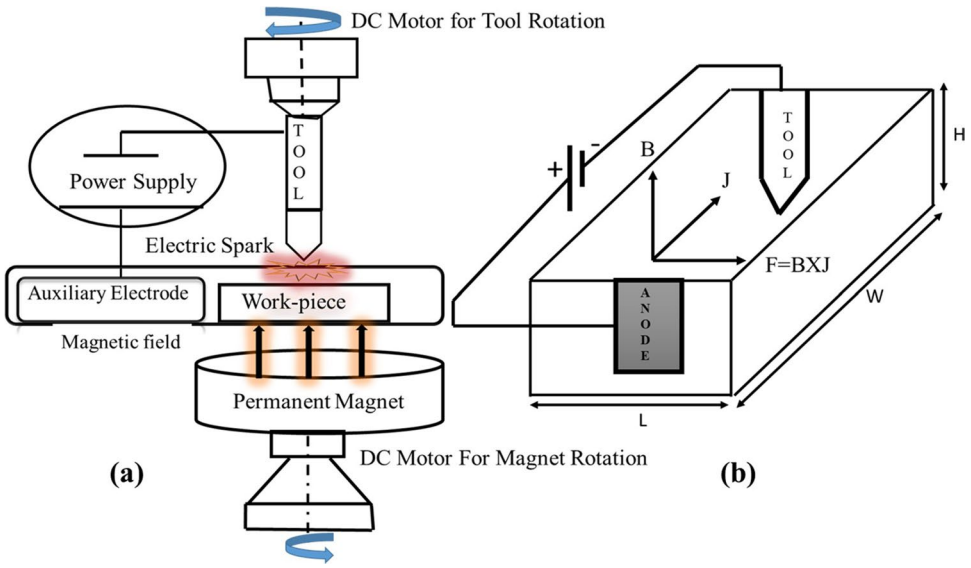

Fig. 1 Elements of Rotary Magnetic field Assisted ECDM (b) Force Components

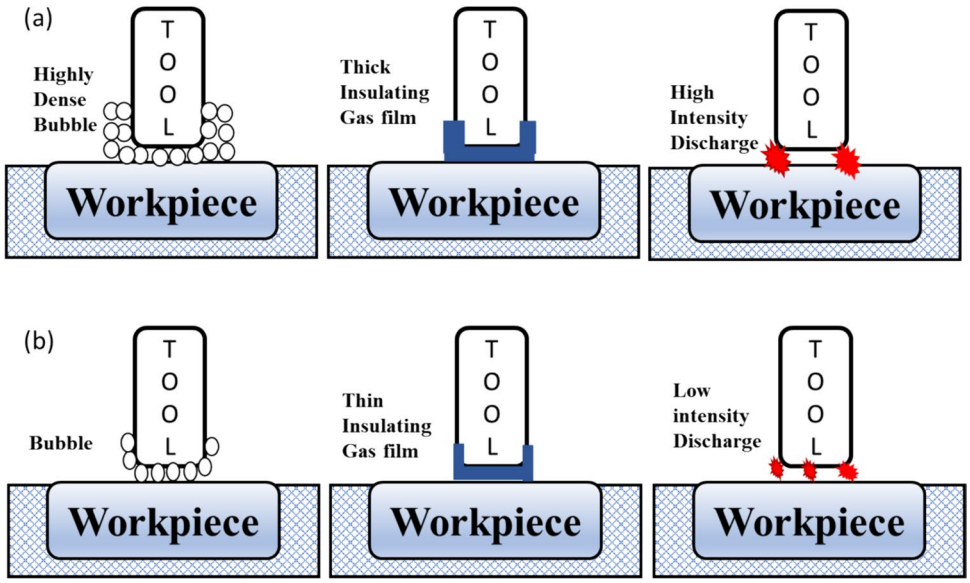

Fig. 2 Bubble generation, gas film formation, and discharge (**a**) Non-MHD (**b**) MHD convection

steering impact enhances the bubble growth and detachment cycle stages. Figure 2 shows the development, formation, and discharge phenomena with and without the magnetic field. Bubble departure radius, film thickness, and spark intensity decrease with the association of a magnetic flux, which is mainly responsible for enhancing the response parameters (Fig. 2 a and b). It also impacts the critical voltage required to initiate the discharge.

The necessary voltage to create the spark decreases with the magnetic field and obtains an earlier release of low-intensity spark. The discharge under MHD convection (Fig. 3a) is mainly responsible for the workpiece's thermal softening and chemical etching. The uniform spark is attained by applying a rotary magnetic field focused on a localized gap domain. It will also improve the thermal damage and cracks by reducing breakdown voltage and heat energy.

The direction of various forces originates from MHD convection synchronization by a rotary magnetic field supporting uniform discharge. Mainly, it induces the steering effect, which minimizes the film thickness and bubble detainment radius, enhancing discharge frequency and intensity due to thin gas film formation. This MHD convection influences the hydrodynamic regime. This paper used a silica glass slab of 75x25x1.3 mm to perform the experiments.

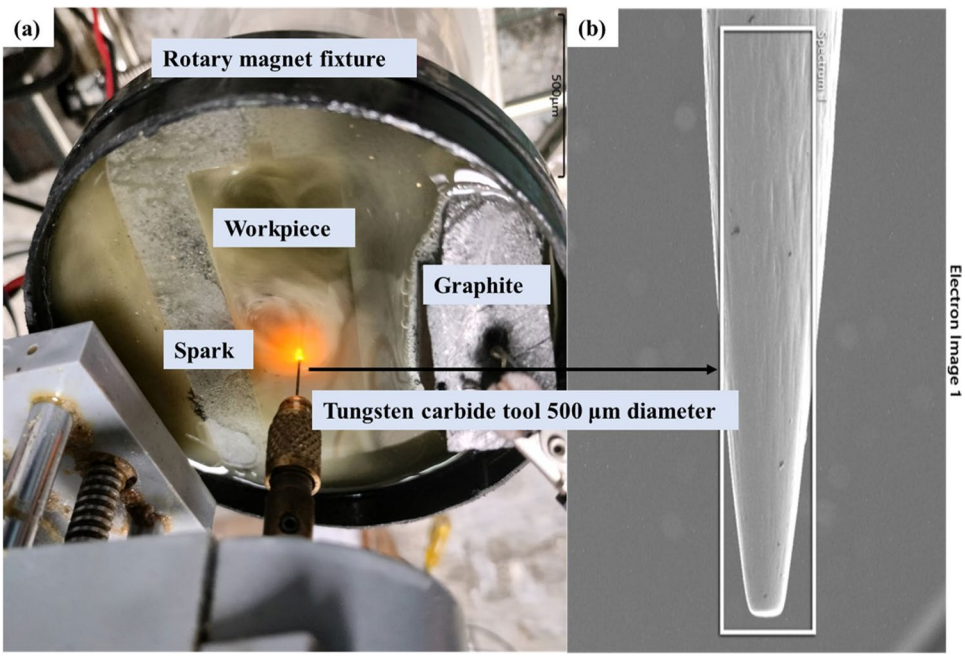

Fig. 3 **a**. Spark Formattion the RMAECDM process **b**. WC Microtool with taper angle

The machining container (250 X 250 X 50mm) is made of a transparent acrylic sheet to visualize discharge phenomena and machining progress (Fig. 3). It contains a fixture to hold the job, secondary electrode mounting, and cover to prevent chemical west to the surroundings. Graphite is used as an auxiliary electrode and connects with the positive terminals of the power supply. The negative terminal of the power supply is associated with the tool made of tungsten carbide (500µm diameter), as shown in Fig. 3b. The cup grinding wheel attachment is attached to the lathe machine for microtool manufacturing in-house. When the electrochemical reactions start, the oxygen bubble forms near the anode, and a hydrogen gas bubble forms near the cathode surface. Voltage, concentration, magnetic field strength, and rotation were controllable variables. The range of controllable parameters is decided based on pilot experiments and a literature review, as given in the table. MRR and WOC are calculated by

$$MRR = \frac{W_1 - W_2}{t} \tag{1}$$

$$WOC = W_{channel} - D_t \tag{2}$$

Where, W_1, W_2, and t are the initial weight, final weight, and machining time, $W_{Channel}$, the channel width after machining, and D_t is the diameter of the tool.

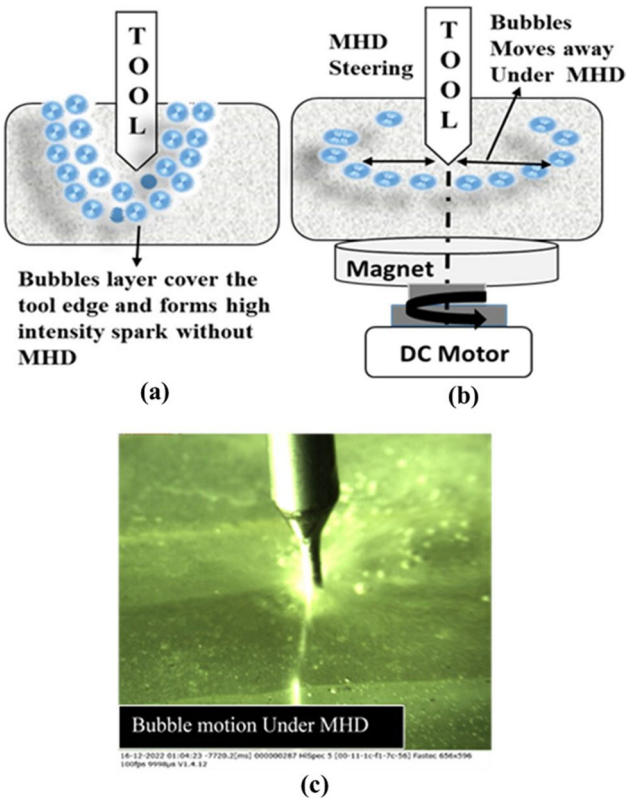

Fig. 4 Bubble & Tool Interaction (**a**) Non-MHD (**b**) With MHD (**c**) High-speed image of bubble dispersion under MHD

3 Mechanism of the Process

In the RMAECDM process, the primary cause of the process improvements is the synchronized steering effect on the gas bubble and film formation. It maintains uniform spark intensity and increases the spark frequency.

This coordinated steering effect is encouraged due to the Lorentz force acting on the conductive medium, which originated from the combined effect of static electric and rotary magnetic fields. The magnetic field continuously changes the Lorentz force direction, maintaining uniform pressure on the gas film. Hydrogen and oxygen gas bubble formation initiates on the periphery of the cathode and anode after a particular value of critical voltage and covers it (Fig. 4a). This covered area behaves as a dielectric medium. The concentrated spark at the sharp edge of the tool provides good precision and minimum overcut. This high-intensity spark is mainly responsible for increasing the chemical etching rate by breaking the silicon bond in the glass surface. The chemical etching rate depends on the surface temperature induced by a continuous spark in the gap.

The etched material remains stuck on the surface at higher depths during machining, which prevents the high aspect ratio microchannel and micromole from being obtained. Researchers applied various techniques for the debris ejection, i.e., tool sonification, tool rotation, static magnetic field, and workpiece table movements.

This work used a novel approach of rotary magnetic field with the ECDM setup to fabricate the microchannel. It induces extra thrust for debris removal from the gap under a synchronized magnetic field. Figure 5 shows the bubbles and gas film formation at different time steps taken using a high-speed camera. It also represents the adhesion action with the tool edge without a magnetic field. The circular motion of the bubble decreases the adhesion and movements of the bubble toward the cutting edge. As a result, early discharge with low intensity takes place. The exerted force reduces the film thickness and departure radius, further influencing the quality characteristics under the influence of the magnetic field. The bubble formation cycle is completed in three stages, as shown in the schematic diagram. The nucleation initiates at the supersaturation condition. The bubble tries to attach to a small-sized bubble during the growth stages. In the departure stages, buoyancy forces dominate the surface tension and bubble transport away from the electrode surface. It moves in the bulk zone after separating from the tool-electrolyte interface. The departure stages of the bubble significantly affect the discharge frequency

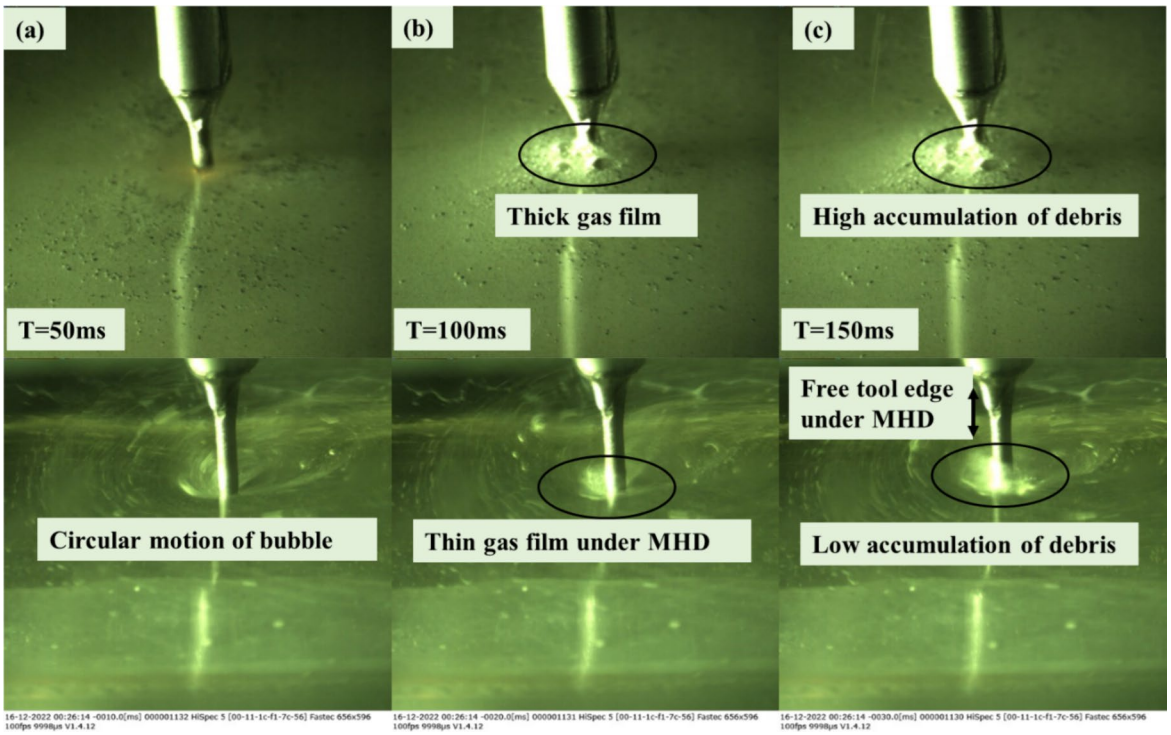

Fig. 5 Bubble and gas film with magnetic and non-magnetic field (**a**) 50ms (**b**) 100ms (**c**) 250ms

and intensity. The lower departure radius increases the discharge frequency and decreases the power of the spark. The rotary magnetic field induces hydrodynamic convection, giving a steering effect to the bubble, which follows the mathematical relation of $F_L = J \times B$ (F_L, J and B are the Lorentz force, current density, and the magnetic flux). The variation of electric potential and magnetic flux controls the steering action induced. The film formation and bubble growth stages change precisely with varying magnetic field strength and rotational speed. It increases the interaction of fresh electrolytes with the tool and influences the current density. The process becomes more capable of fabricating high aspect ratio channels, which is difficult with the conventional manner of ECDM. The disturbance of film and bubble formation increases with changes in the strength and rotation of the magnetic field. It provides absolute real-time control of process parameters by minimizing the discharge intensity and increasing the frequency. The bubble separation rate depends on the direction of Lorentz and buoyancy force (Fig. 6). When F_b and F_L In the same direction, the aggregate outcome will increase the bubble separation rate (Fig. 6). It also decreases the departure size compared to the non-magnetic field. The mathematical relation for several forces under the impact of the magnetic strength are

$$F_b + F_L = F_s \tag{3}$$

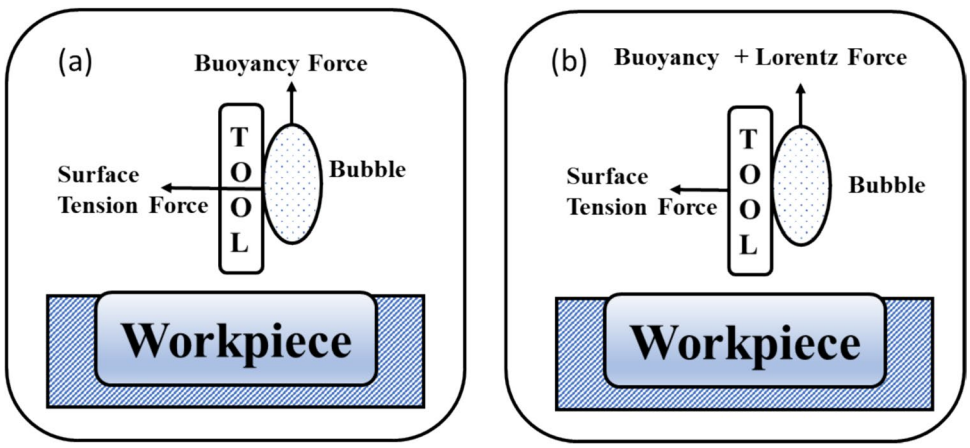

Fig. 6 Element of Force (**a**) Without magnetohydrodynamic (**b**) With Magnetohydrodynamic

$$F_b = \frac{\pi}{6} d^3 (\rho_l - \rho_g) g \tag{4}$$

$$F_s = \pi d_c \gamma sin\alpha \tag{5}$$

Where ρ_l, ρ_g are the density of the gaseous phases and liquid phases, α is the contact, and d_c Contact bubble diameter with the electrode, γ, surface tension. The bubble detachment phenomena from the tool-electrolyte interface changes with the forces discussed in Eqs. 3, 4 and 5. Bubble growth and detachment are mainly governed by force (F_b) without MHD convection. F_s empowers the bubbles, holding them until the F_b, and departure size becomes sufficiently large to overwhelm them. MHD convection impacts the bubble departure radius process and alters the gaseous product, which decreases the electrode potential. The circular-like motion directed through the Lorentz force produces minuscule vortices and induces MHD convection of the electrolyte. It influences the mass transfer, ion movement, electrochemical dissolution, and bubble formation stages. Magnetic flux contributed significantly to the mass transfer process, changing the movement of gas-phase products and reducing electrode potential.

3.1 Modelling Studies of MHD Convection in RMAECDM

The velocity component due to Lorentz force is determined using the Navier stroke equation to find the effect of magnetic field strength on the electrolyte steering. The external force component, i.e., Lorentz force, becomes zero whenever no magnetic flux is applied.

Without MHD convection

$$\rho \frac{\partial Ur}{\partial t} + u\left(\frac{\partial \mathrm{Ur}}{\partial r}\right) = -\frac{\partial \mathrm{P}}{\partial \mathrm{r}} \tag{6}$$

With MHD convection

$$\rho \frac{\partial Ur}{\partial t} + u\left(\frac{\partial \mathrm{Ur}}{\partial \mathrm{r}}\right) = -\frac{\partial \mathrm{P}}{\partial \mathrm{r}} + J \times B \tag{7}$$

Equations (6) and (7) represent the governing equation to analyze the effect of the external force component on the electrolyte velocity with and without the magnetic field. Lorentz force is obtained by coupling the Navier stroke and Laplace equations with the known magnetic field

$$J = \sigma \nabla \varnothing \tag{8}$$

Laplace equation [42] (Eq. 8) was solved in the first stage to find the potential distribution and current density vector with the following boundary conditions [43].

B.c's

$$B.c's \ \varnothing = 0 \ (Tool\ surface), \ \varnothing = V \ (Anode), \ \frac{\partial \varnothing}{\partial n} = 0 \ (insulating\ surface) \tag{9}$$

The simplified model represents the relation between Lorenz force (Fl), buoyancy force (F_b), and surface tension force (F_s).

$$\mathrm{F}_b + \mathrm{F}_l = \mathrm{F}_s \tag{10}$$

Lorenz force induces the MHD convection in the electrolyte. The departure radius of the hydrogen bubble from the electrode with a magnetic field is given by [44]

$$\mathrm{Rd} = \sqrt{\frac{\mathrm{C}_s \sigma - 4(J \times \mathrm{B})}{\mathrm{C}_b \ \mathrm{g}(\rho_b - \rho_g)}} \tag{11}$$

The departure radius of hydrogen bubbles without a magnetic field is

$$\mathrm{Rd} = \sqrt{\frac{Cs\sigma}{\mathrm{C}_b \ \mathrm{g}(\rho b - \rho g)}} \tag{12}$$

Where, ρ_b is the bulk flow density. C_b and C_s are constant coefficients and ρ_g is the hydrogen bubble density. Electrolyte flow velocity depends on the magnitude of Lorenz's force. The model computes the impact of magnetohydrodynamic convection on bubble size.

4 Results and Discussion

4.1 Regression Model and Analysis of Variance for MRR and WOC

A regression model was developed to examine the outcome of different input parameters on MRR and WOC. The model summary indicates a significant contribution of the input parameters.

$$MRR = -0.0884 + 0.000391 * \mathrm{A} + 0.001069 * \mathrm{B} + 0.0046 * \mathrm{C} + 0.000364 * \mathrm{D} \tag{13}$$

$$WOC = -0.5162 + 0.000988 * \mathrm{A} + 0.001747 * \mathrm{B} + 0.00894 * \mathrm{C} + 0.001199 * \mathrm{D} \tag{14}$$

Constraints in terms of the bounded value of the problem given by Eqs. 13 and 14 are

$$220mT < A < 330mT, \ 10 < B < 30, \ 38(V) < 42(V), \ 10(\%) < D < 20(\%) \tag{15}$$

A, B, C, and D are the magnetic strength, rotation, voltage, and concentration. Equations 13 and 14 were the objective function followed by the constraints (Eq. 15) to obtain the optimal setting of output variables.

Table 1 shows the model summary in terms of R^2 value indicates the excellent agreement of the regression model

Table 1 Model Summary of MRR and WOC

Response	S	R-sq	R-sq(adj)	R-sq(pred)
MRR	0.0117958	83.76%	78.76%	66.36%
WOC	0.0138673	95.40%	93.99%	90.84%

Table 2 Analysis of Variance for WOC

Source	DF	Adj SS	Adj MS	F-Value	P-Value
Regression	4	0.051901	0.012975	67.47	0.000
Magnetic Strength(T)	1	0.043966	0.043966	228.63	0.000
Rotation (Thousand)	1	0.003663	0.003663	19.05	0.001
Voltage	1	0.003840	0.003840	19.97	0.001
Concentration	1	0.000431	0.000431	2.24	0.158
Error	13	0.002500	0.000192		
Total	17	0.054401			

Table 3 Analysis of Variance for MRR

Source	DF	Adj SS	Adj MS	F-Value	P-Value
Regression	4	0.009330	0.002332	16.76	0.000
Magnetic Strength(T)	1	0.006882	0.006882	49.46	0.000
Rotation (Thousand)	1	0.001372	0.001372	9.86	0.008
Voltage	1	0.001036	0.001036	7.45	0.017
Concentration	1	0.000040	0.000040	0.29	0.602
Error	13	0.001809	0.000139		
Total	17	0.011138			

with the experimental observation of MRR and WOC. The F value (Tables 2 and 3) of magnetic strength is highest for the MRR and width of the cut, indicating that it provides more impact, followed by voltage, rotation, and concentration. The magnetic field strength directly impacts the electrolyte steering, which is responsible for the earlier and low-intensity discharge. It also increases the discharge frequency due to lower film formation under MHD convection.

5 Stirring effect of the electrolyte under MHD convection by rotating magnet

Experiments were conducted to investigate the electrolyte stirring effect with and without a magnetic field. Microparticles removed from the workpiece after machining try to accumulate around the tool edge, as shown in Fig. 7a. They resist the current flow, and machining will stop after a certain depth. Discharge frequency decreases due to a higher value of critical voltage. Figure 7b shows the particle removed from the workpiece moving away under magnetic field influence and rotating counter-clockwise. They spread outward during the microfabrication process under the influence of a magnetic field, which implies that the magnetic field promotes the electrolyte's movement. Early discharge takes place due to the reduction of the critical voltage. The trajectory of charged ions and movements will change under the MHD convection caused by an alternating magnetic and electric flux. It increases their collision probability with other molecules and enhances the electrolyte's mass transfer rate. Due to the electrolyte steering, the bubble moves away from the machining zone. As a result, fresh electrolytes come in contact and increase the chemical reaction. This effect can decrease gas film thickness, increase the bubble's departure frequency, and provide uniform discharge. All these improve the machining rate and accuracy of microfabrication by the ECDM process.

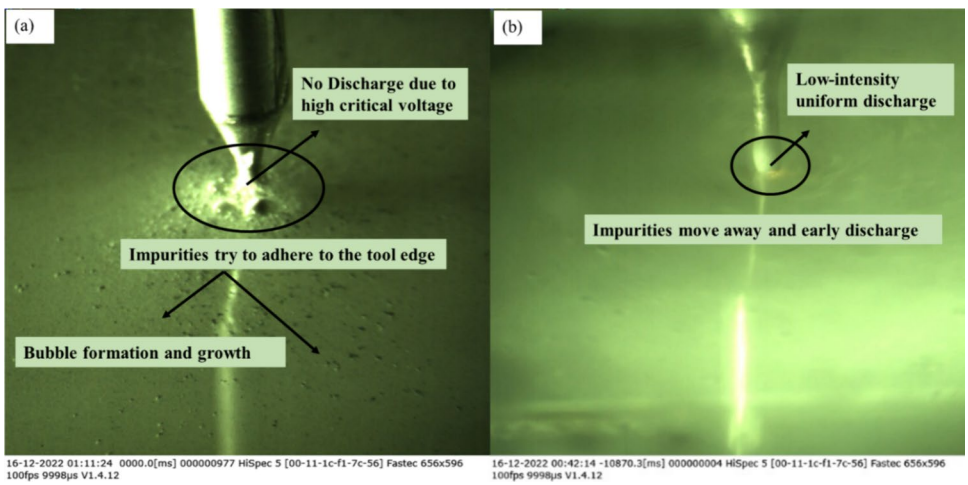

Fig. 7 High-speed images of bubble entrapment phenomena and discharge during microchannel fabrication (**a**) Non-Magnetic field (**b**) Magnetic field

5.1 Effect of Magnetic Flux Density on Performance Characteristics

When the magnetic flux strength is less than 0.05T, the impact of MHD convection is weak, and the motions of the charged ion are slightly exaggerated. The effect of the feeble magnetic flux declined towards process enhancements. The mean level of the magnetic field (.05 to .1) induces more vital Lorentz force, which makes the radii of spinning motion trajectories longer. Thus, the collision between ions and other molecules will increase and cause more steering impact. It will improve mass transfer and depth of machining in the ECDM process. With magnetic strength that is too high (.15 to .2 T), more extended spiral motion and trajectory are obtained due to the Lorentz force. It will throw away the ions from the reaction area and cannot participate in the chemical etching.

Figure 8 a, b, and c show the effect of static and dynamic magnetic fields on the surface generated during microchannel fabrication. It shows that in a non-magnetic field, there is incomplete machining due to the high resistance created by the accumulated impurities on the tool edge (Fig. 7a and Fig. 8a). Complete machining up to the desired depth with nonuniform surface generation and microcracks is possible with the static magnetic field. In contrast, uniform machining without cracks is obtained with a rotary magnetic field. In addition to this, rotary magnetic fields remove more material than static and non-rotating magnetic fields. The interaction of the field with local current density produces a flow that tend to diminish thickness of diffusion layer while increasing mass transfer [45].

5.2 Effect of magnetic flux density on MRR and WOC

Figures 10 and 11 show the increasing trends of material removal rate and width overcut with the magnetic strength. Lorentz force increases with the magnetic field, which induces more MHD effects due to the rotation of the bubble around the tooltip. Due to the steering action, the bubble starts to move away from the tool tip, which is responsible for increasing the chemical reaction and molecular interaction since additional fresh electrolytes come in contact with the tooltip, and the rate of chemical reaction increases. The departure radius and bubble stay time on the tooltip also decrease, which assists in focusing the spark in a confined region and improves the discharge rate. It increases the MRR and decreases the WOC

5.3 Effect of magnetic field rotation on MRR and WOC

Figures 9 and 10 show the increasing trends of MRR and WOC with the magnetic field rotation. The tabula results also show the rising trends of MRR and WOC with magnetic field rotation. When a magnetic field is applied to an electrochemical cell, it acts on the charged species with the current density (j) to generate the Lorentz force $F_{L,}$ which induces MHD convection. The alternating magnetic field is generated by spinning the permanent magnet with the DC motor attached to the experimental setup. It provides higher machining accuracy than the stationary magnetic field. The Lorentz force is directly proportional to the magnetic field strength. A higher magnetic field creates more suction, which separates the gas bubble from the tooltip (Fig. 6c). The rotary magnetic field provides sufficient suction time to move away the bubble from the tooltip, which is responsible for generating a uniform surface. MRR and WOC's growth rate is higher at the initial level (10000 to 20000 rpm). After the saturation state, the increment of MRR and WOC decreases. As the bubble moves away from the tool, suction is created. As a result, the fresh electrolyte supplies in the gap created due to the bubble movements. The alternating magnetic field

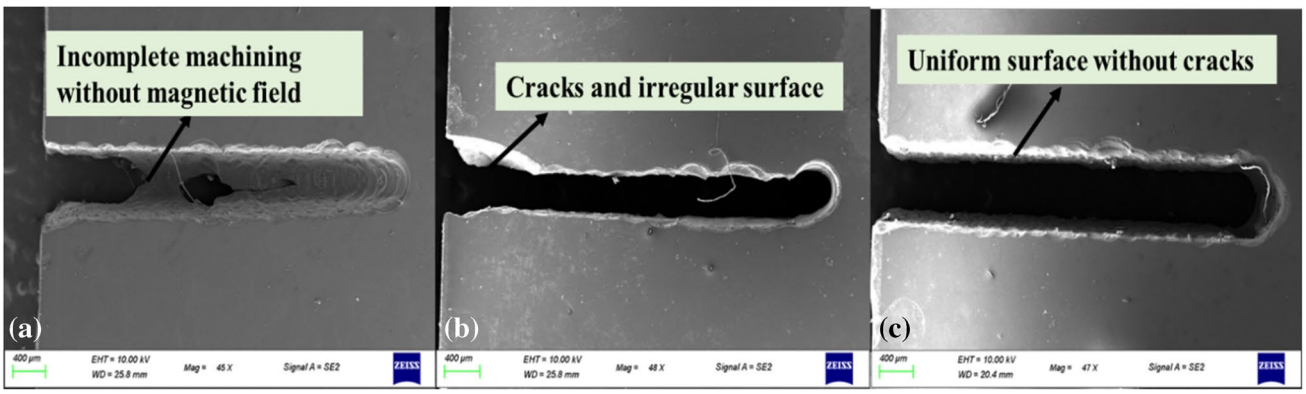

Fig. 8 Microchannel fabrication at (**a**) Non-Magnetic (**b**) Static Magnetic (**c**) Rotary Magnetic

Fig. 9 Variation of WOC with the input parameters

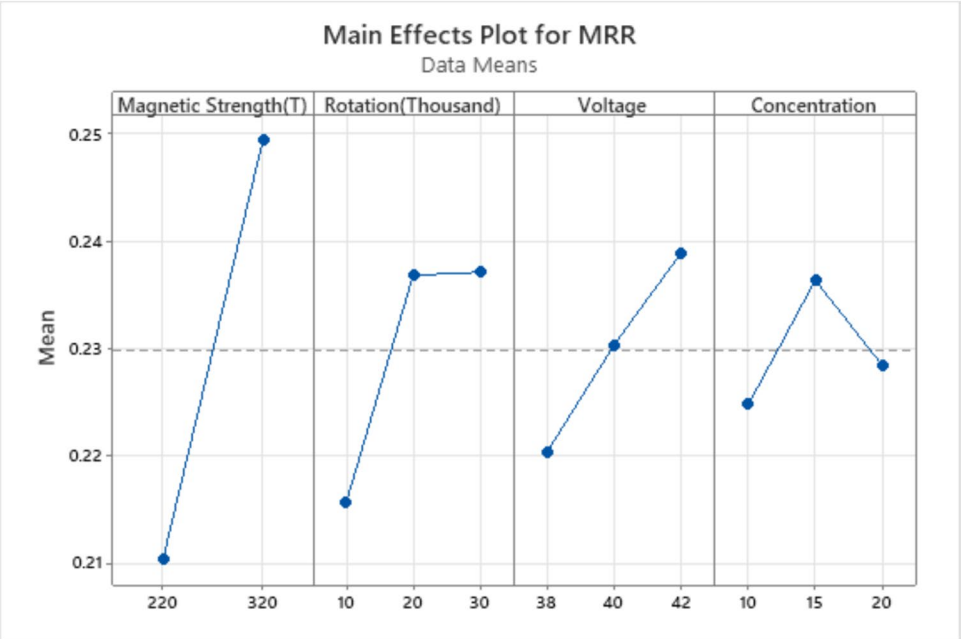

Fig. 10 Variation of MRR with the input parameters

allows more time for electrolyte molecules to participate in the chemical reaction. It will increase the discharge energy and MRR.

5.4 Effect of voltage on MRR and WOC

The rising trend of MRR and WOC with voltage are shown in Figs. 9 and 10. Higher discharge energy is available with increasing the voltage. The Lorentz force increases with the voltage since it increases the electrolyte current flow. With a higher Lorentz force, a more significant MHD effect induces bubble rotation around the tooltip. The bubble's departure radius and residence time on the tooltip also decrease, which helps to concentrate the spark in a confined region and improve discharge frequency. Lorentz force produces more suction effect around the tool. The departure radius and gas film thickness are reduced by the Lorentz force. It increases the discharge frequency, which is responsible for increasing the MRR and WOC.

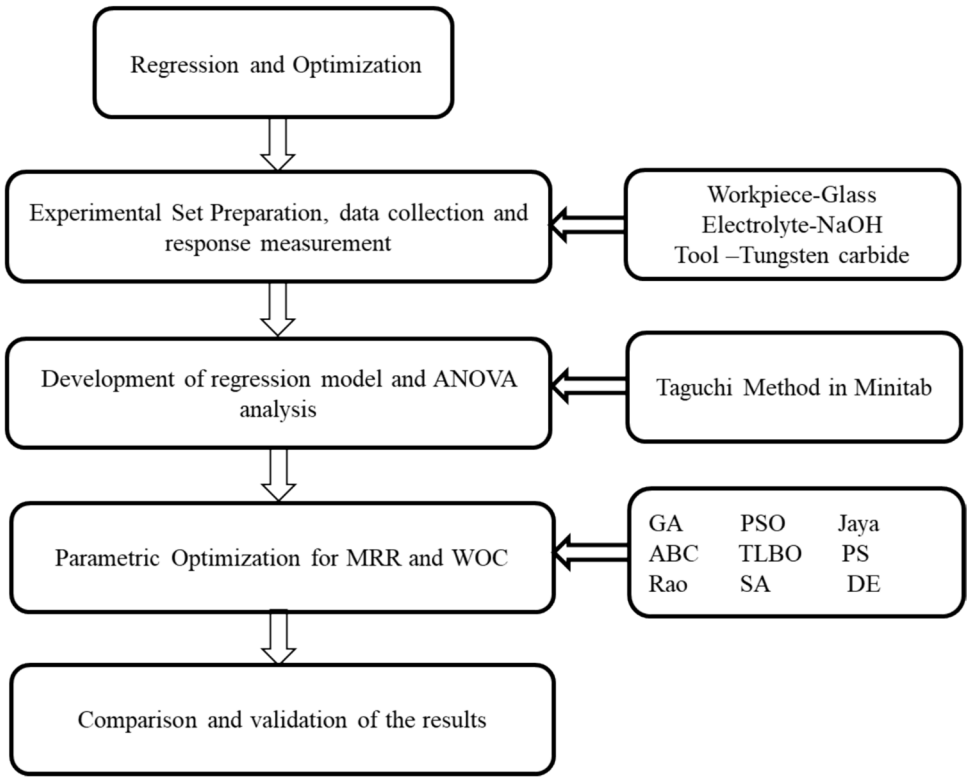

Fig. 11 Flow Diagram for regression and optimization

5.5 Effect of concentration on MRR and WOC

Figures 9 and 10 show the effect of MRR and overcut with electrolyte concentration. The trend followed by output parameters with an increase in voltage can be observed as almost consistent with the advance in concentration. Spark intensity increases with increasing electrolyte concentration (10% to 15 % by weight), advancing the MRR from 0.227 mg/min to 0.234 mg/min, and the overcut from 149.665µm to 162.6228µm due to electrolyte ions increments. The number of ions increases with the concentration, resulting in a high spark intensity at the machining zone, which increases MRR and WOC.

5.6 Optimization using nature-inspired algorithms

Steps required to find the optimal solution with the hybridization of the Taguchi method and nature-inspired algorithms are shown in Fig. 11. MRR and WOC are considered output and parametric optimization using nature-inspired algorithms carried out in this work for obtaining the optimal set of input parameters. The regression model obtained by the Taguchi method acts as an objective function, and the range of each parameter is considered a bounded value. The results of different nature-inspired algorithms are compared for the appropriate selection of algorithms (Table 4).

Figure 12 shows the complete procedure using a flow diagram to find the optimal solution using nature-inspired algorithms. Steps include population initialization and termination. If further improvements are impossible, a randomly selected solution is checked and finalized in the following steps. Table 4 shows that convergence obtained

Table 4 Fitness value by various optimization algorithms

Optimization Techniques	Responses	Number of Iteration	Fitness Value
GA	MRR	91	**0.3144**
	WOC	51	**0.07034**
Pattern Search	MRR	52	0.3144
	WOC	20	0.07034
Simulated Annealing	MRR	2970	0.3142
	WOC	2000	0.07034
PSO	MRR	10	.3144
	WOC	25	0.07034
ABC	MRR	2000	0.3132
	WOC	6500	.0740
TLBO	**MRR**	**10**	**0.3144**
	WOC	**10**	**0.07034**
Jaya	MRR	10	0.3144
	WOC	15	0.07034
DE	MRR	50	0.3144
	WOC	20	0.07034
Rao	MRR	20	0.3144
	WOC	5	0.07034

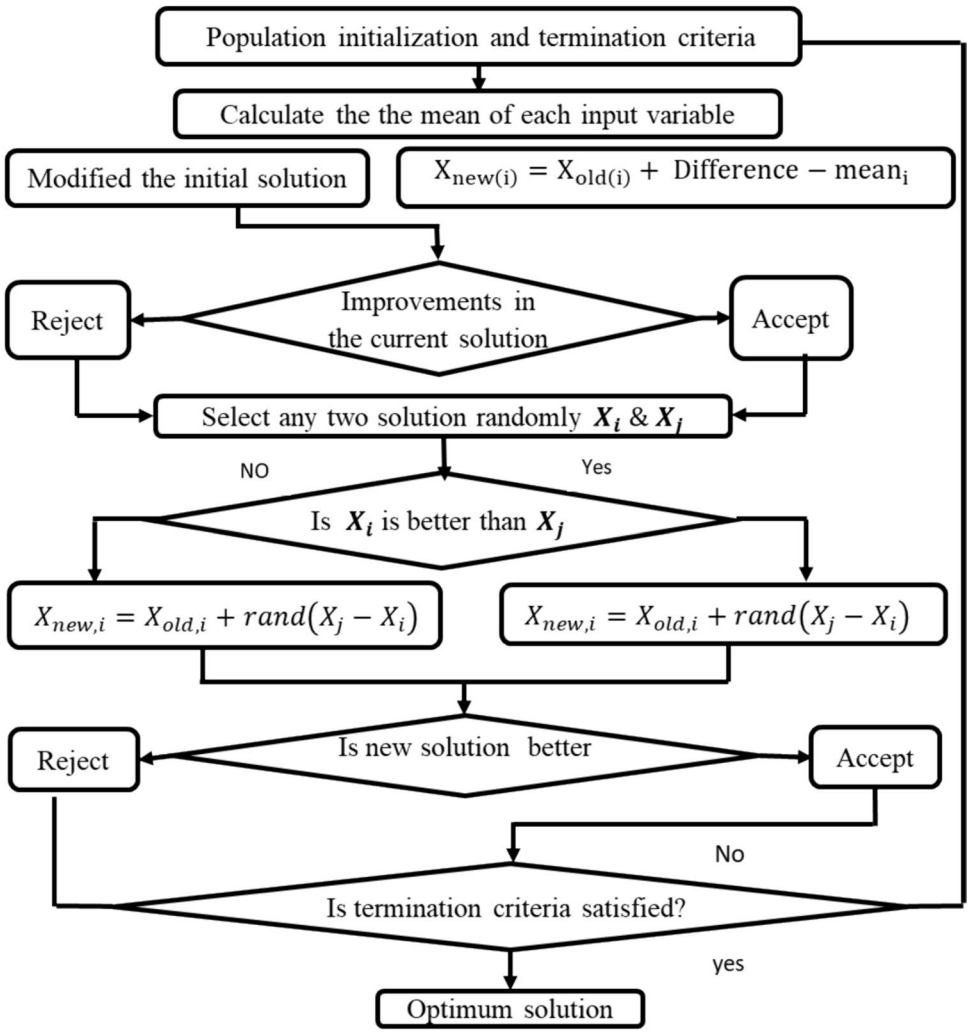

Fig. 12 Flow Chart for optimization using Nature-inspired algorithms

Table 5 Validation of optimization results obtained by nature-inspired algorithms

S. No.	Responses	Optimum fitness value obtained by algorithms	Validation experimental value	% Error
1	MRR	0.3144	.2977	5.311
2	WOC	0.07034	.06651	5.44

by various algorithms to reach the optimal solution differs. The TLBO algorithms converge the optimal solution of MRR and WOC more quickly than other nature-inspired algorithms. Table 5 shows the results of the validation experiments and the error analysis. No significant difference exists between the experimental and optimum results of nature-inspired algorithms

Table 6 Comparison of WOC at different working conditions

Exp.	Conventional ECDM	Static magnetic field ECDM	Rotary magnetic field ECDM
1	0.0943mm	0.0798mm	0.0734mm
2	0.0941mm	0.0792mm	**0.0731mm**
3	0.0946mm	0.0797mm	0.0738mm

5.7 Comparison of Conventional ECDM, Static Magnetic Field, and Rotary Magnetic Field Assisted ECDM for WOC

A comparative study of static magnetic field, dynamic magnet field, and traditional ECDM process was carried out by

performing the experiments. Table 6 shows the significant improvement of quality characteristics in the ECDM process by applying a dynamic magnetic field compared to static and conventional ECDM processes.

6 Conclusions

1. The novel approach of the rotary magnetic field in the ECDM is proposed to study the effect of MHD convection due to rotary magnetic field on bubble growth, departure, and film formation. It directly influences the response characteristics.
2. Modelling studies were carried out to find the effect of the rotary magnetic field on the performance characteristics of the ECDM process.
3. The experiments were conducted with a rotating magnetic field in the ECDM process, and responses were measured to develop the mathematical model. The model explains the impact of the rotary magnetic field on performance characteristics. The result shows the significant contribution of magnetic field rotation and strength on the width of the cut and MRR. The MHD convection provides earlier discharge of low intensity due to thin film formation, which increases the process's capability to fabricate a high aspect ratio microchannel.
4. A comparison of conventional ECDM, static magnetic field assisted ECDM, and rotary magnetic field ECDM was also carried out. Improvements in MRR and WOC are observed with the application of rotary magnetic field in comparison to conventional ECDM and static magnetic field assisted ECDM process.
5. Nature-inspired algorithms were implemented to find the optimal setting of input parameters. Response parameters obtained by these algorithms are 0.3144 and 0.07034mm. The optimal setting of input parameters for minimizing WOC is 220mT (magnetic field strength),20000 rpm(rotation),40V(voltage), and 10%(concentration), which are further verified by validation experiments.

Acknowledgments The author(s) would like to thank Indian Institute of Technology Roorkee(IITR), Uttarakhand, India for providing valuable lab support for conducting experiments

Author Contributions All authors contributed to the study conception and design. Material preparation, data collection and analysis were performed by [Dilip Gehlot], [Prof. Pradeep Kumar Jha] and [Prof. Pramod Kumar Jain]. The first draft of the manuscript was written by [Dilip Gehlot] and all authors commented on previous versions of the manuscript. All authors read and approved the final manuscript.

Funding The authors declare that no funds, grants, or other support were received during the preparation of this manuscript.

Data availability No datasets were generated or analysed during the current study.

Declarations

Ethics Approval Not applicable

Consent to Participate Not applicable

Consent to Publication Not applicable

Competing Interests The authors declare no competing interests.

References

1. Jain VK, Choudhury SK, Ramesh KM (2001) On the machining of alumina and glass. Int J Mach Tools Manuf 42:1269–1276
2. Maillard P, Despont B, Bleuler H, Wüthrich R (2007) Geometrical characterization of micro-holes drilled in glass by gravity-feed with spark assisted chemical engraving (SACE). J Micromechanics Microengineering 17(7):1343–1349. https://doi.org/10.1088/0960-1317/17/7/017
3. Abou Ziki JD, FatanatDidar T, Wüthrich R (2012) Micro-texturing channel surfaces on glass with spark assisted chemical engraving. Int J Mach Tools Manuf 57:66–72. https://doi.org/10.1016/j.ijmachtools.2012.01.012
4. Furutani K, Maeda H (2008) Machining a glass rod with a lathe-type electro-chemical discharge machine. J Micromechanics Microengineering 18(6). https://doi.org/10.1088/0960-1317/18/6/065006.
5. Bhuyan BK, Yadava V (2014) Experimental study of traveling wire electrochemical spark machining of borosilicate glass. Mater Manuf Process 29(3):298–304. https://doi.org/10.1080/10426914.2013.852216
6. Khairy ABE, McGeough JA (1990) Die-Sinking by Electro-erosion-Dissolution Machining. CIRP Ann – Manuf Technol 39(1):191–195. https://doi.org/10.1016/S0007-8506(07)61033-6
7. Jain VK, Chak SK (2000) Electrochemical spark trepanning of alumina and quartz. Mach Sci Technol 4(2):277–290. https://doi.org/10.1080/10940340008945710
8. Singh T, Dvivedi A (2016) International Journal of Machine Tools & Manufacture Developments in electrochemical discharge machining : A review on electrochemical discharge machining, process variants and their hybrid methods. Int J Mach Tools Manuf 105:1–13. https://doi.org/10.1016/j.ijmachtools.2016.03.004
9. Sarkar BR, Doloi B, Bhattacharyya B (2006) Parametric analysis on electrochemical discharge machining of silicon nitride ceramics. Int J Adv Manuf Technol 28(9):873–881. https://doi.org/10.1007/s00170-004-2448-1
10. Wu R (2006) The gas film in spark assisted chemical engraving SACE) — A key element for micro-machining applications. 46: 828–835 https://doi.org/10.1016/j.ijmachtools.2005.07.029
11. Liu JW, Yue TM, Guo ZN (2010) International Journal of Machine Tools & Manufacture An analysis of the discharge mechanism in electrochemical discharge machining of particulate reinforced metal matrix composites. Int J Mach Tools Manuf 50(1):86–96. https://doi.org/10.1016/j.ijmachtools.2009.09.004
12. Han MS, Min BK, Lee SJ (2008) Modeling gas film formation in electrochemical discharge machining processes using a side-insulated electrode. J Micromechanics Microengineering. 18(4). https://doi.org/10.1088/0960-1317/18/4/045019

13 Wüthrich R, Bleuler H (2004) A model for electrode effects using percolation theory. Electrochim Acta 49:1547–1554. https://doi.org/10.1016/j.electacta.2003.11.014

14. Kulkarni A, Sharan R, Lal GK (2022) An experimental study of discharge mechanism in electrochemical discharge machining. Int J Mach Tools Manuf 42:1121–1127

15. Basak I, Ghosh A (1996) Mechanism of spark generation during electrochemical discharge machining: A theoretical model and experimental verification. J Mater Process Technol 62(1–3):46–53. https://doi.org/10.1016/0924-0136(95)02202-3

16. Zou Z et al (2023) Electrochemical discharge machining of a high-precision micro-holes array in a glass wafer using a damping and confinement technique. J Manuf Process 99:152–167. https://doi.org/10.1016/j.jmapro.2023.05.031

17. Huang SF, Liu Y, Li J, Hu HX, Sun LY (2014) Electrochemical discharge machining micro-hole in stainless steel with tool electrode high-speed rotating. Mater Manuf Process 29(5):634–637. https://doi.org/10.1080/10426914.2014.901523

18. Han MS, Min BK, Lee SJ (2007) Improvement of surface integrity of electro-chemical discharge machining process using powder-mixed electrolyte. J Mater Process Technol 191(1–3):224–227. https://doi.org/10.1016/j.jmatprotec.2007.03.004

19. Jain VK, Choudhury SK, Ramesh KM (2002) On the machining of alumina and glass. Int J Mach Tools Manuf 42(11):1269–1276. https://doi.org/10.1016/S0032-3861(02)00241-0

20. Cheng CP, Wu KL, Mai CC, Hsu YS, Yan BH (2010) Magnetic field-assisted electrochemical discharge machining. J Micromechanics Microengineering 20(7). https://doi.org/10.1088/0960-1317/20/7/075019

21. Wüthrich R, Despont B, Maillard P, Bleuler H (2006) Improving the material removal rate in spark-assisted chemical engraving (SACE) gravity-feed micro-hole drilling by tool vibration J Micromechanics Microengineering 16(11). https://doi.org/10.1088/0960-1317/16/11/N03

22. Zhang J, Xu Z, Geng T (2023) Vibration-assisted electrochemical discharge drilling method for microholes without recast layer. Int J Adv Manuf Technol 167–182. https://doi.org/10.1007/s00170-023-12250-y.

23. Chen Z, Liu Y, Wang T, Wang K (2023) Ultrasonic assisted electrochemical discharge milling of complex glass microstructure with high-quality. J Manuf Process 94:94–106. https://doi.org/10.1016/j.jmapro.2023.03.044

24. Arya RK, Dvivedi A (2023) Improving the electrochemical discharge machining (ECDM) process for deep-micro-hole drilling on glass by application of the electrolyte-air injection. Ceram Int 49(6):8916–8935. https://doi.org/10.1016/j.ceramint.2022.11.047

25. Gehlot D, Jha PK, Jain PK (2024) Microchannel Fabrication on Silica Glass and Experimental Investigation of MHD Convection in ECDM Process. Silicon 16(6):2521–2531. https://doi.org/10.1007/s12633-024-02859-3

26. Hajian M, Razfar MR, Movahed S (2016) An experimental study on the effect of magnetic field orientations and electrolyte concentrations on ECDM milling performance of glass. Precis Eng 45:322–331. https://doi.org/10.1016/j.precisioneng.2016.03.009

27. Gehlot D, Jha PK, Jain PK (2023) Experimental Investigation and Modelling Studies on MHD Convection in Magnetic-assisted -ECDM. Mater Manuf Process 00(00):1–12. https://doi.org/10.1080/10426914.2023.2236207

28. Xu Y, Jiang B (2020) Machining performance enhancement of deep micro drilling using electrochemical discharge machining under magnetohydrodynamic effect. Int J Adv Manuf Technol. https://doi.org/10.1007/s00170-021-06657-8/Published

29. Arab J, Dixit P (2023) Gas bubbles entrapment mechanism in the electrochemical discharge machining involving multi-tip array electrodes. J Manuf Process 99:38–52. https://doi.org/10.1016/j.jmapro.2023.05.038

30. Tacken RA, Janssen LJJ (1995) Applications of magnetoelectrolysis. J Appl Electrochem 25(1):1–5. https://doi.org/10.1007/BF00251257

31. Gehlot D, Jha PK, Jain PK (2023) Micro-slit fabrication using magnetic-assisted ECDM and parametric optimization by metaheuristic algorithms. J Brazilian Soc Mech Sci Eng 45(9):1–17. https://doi.org/10.1007/s40430-023-04390-9

32 Wu R (2005) Machining of non-conducting materials using electrochemical discharge phenomenon — an overview Int. J Mach Tools Manuf 45:1095–1108. https://doi.org/10.1016/j.ijmachtools.2004.11.011

33. Han M, Min B, Lee SJ (2008) Modeling gas film formation in electrochemical discharge machining processes using a side-insulated electrode. https://doi.org/10.1088/0960-1317/18/4/045019

34. Kashyap K, Gehlot D, Jain P (2020) Experimental Analysis of Process Parameters in Electro-Chemical Spark Machining and Optimization using NSGA-II. Ind Eng J 13(3). https://doi.org/10.26488/iej.13.3.1219

35. Harugade M, Waigaonkar S, Kulkarni G, Diering M (2021) Experimental investigations of magnetic field-assisted high-speed electrochemical discharge drilling. Mater Manuf Process 00(00):1–12. https://doi.org/10.1080/10426914.2021.2016814

36. Bhargav KVJ, Balaji PS, Sahu RK, Katiyar JK (2023) Exemplary approach using tool rotation-assisted μ-ECDM for CFRP composites machining. Mater Manuf Process 38(3):271–283. https://doi.org/10.1080/10426914.2022.2072879

37. Elhami S, Razfar MR (2018) Effect of ultrasonic vibration on the single discharge of electrochemical discharge machining. Mater Manuf Process 33(4):444–451. https://doi.org/10.1080/10426914.2017.1328113

38. Elhami S, Razfar MR (2017) Analytical and experimental study on the integration of ultrasonically vibrated tool into the micro electrochemical discharge drilling. Precis Eng 47:424–433. https://doi.org/10.1016/j.precisioneng.2016.09.015

39. Rattan N, Mulik RS (2017) Improvement in material removal rate (MRR) using magnetic field in TW-ECSM process. Mater Manuf Process 32(1):101–107. https://doi.org/10.1080/10426914.2016.1176197

40. Yang CK, Cheng CP, Mai CC, Cheng Wang A, Hung JC, Yan BH (2010) Effect of surface roughness of tool electrode materials in ECDM performance Int J Mach Tools Manuf 50(12): 1088–1096. https://doi.org/10.1016/j.ijmachtools.2010.08.006

41. Jiang B, Lan S, Ni J, Zhang Z (2014) Experimental investigation of spark generation in electrochemical discharge machining of non-conducting materials. J Mater Process Technol 214(4):892–898. https://doi.org/10.1016/j.jmatprotec.2013.12.005

42. Jain VK, Gehlot D (2015) Anode shape prediction in through-mask-ECMM using FEM. Mach Sci Technol 19(2):286–312. https://doi.org/10.1080/10910344.2015.1018533

43. Jain P, Ghelot D, Bagoriya T (2017) Experimental Study of Anode Shape Prediction in Through Mask Electrochemical Micro Machining. 137: 220–228. https://doi.org/10.2991/iccasp-16.2017.36

44. Xu Y, Jiang B (2021) Machining performance enhancement of deep micro drilling using electrochemical discharge machining under magnetohydrodynamic effect. Int J Adv Manuf Technol 113(3–4):883–892. https://doi.org/10.1007/s00170-021-06657-8

45. Monzon LMA, Coey JMD (2014) Magnetic fields in electrochemistry: The Lorentz force. A mini-review. Electrochem Commun 42:38–41. https://doi.org/10.1016/j.elecom.2014.02.006